

ADDING A SUITE OF CHEMICAL ABUNDANCES TO THE MACER CODE FOR THE EVOLUTION OF MASSIVE ELLIPTICAL GALAXIES

ZHAOMING GAN¹, ENA CHOI², JEREMIAH P. OSTRICKER², LUCA CIOTTI³, SILVIA PELLEGRINI³

¹Shanghai Astronomical Observatory, Chinese Academy of Sciences, 80 Nandan Road, Shanghai 200030, China

²Department of Astronomy, Columbia University, 550 W, 120th Street, New York, NY 10027, USA and

³Department of Physics and Astronomy, University of Bologna, via Piero Gobetti 93/2, 40129 Bologna, Italy

Draft version March 20, 2022

ABSTRACT

We add a suite of chemical abundances to the MACER (Massive AGN Controlled Ellipticals Resolved) 2D code, by solving 12 additional continuity equations for H, He, C, N, O, Ne, Mg, Si, S, Ca, Fe and Ni respectively with sources from AGB stars and supernovae of type Ia and II with metal yields based on standard stellar physics. New stars, formed in Toomre unstable circumnuclear disks (of a size $\lesssim 150$ parsec), are assumed to have a top-heavy initial mass function with a power index of 1.65. The metal dilution effects due to cosmic accretion are also included. With the high resolution of few parsecs in central regions, resolved black hole accretion and AGN feedback, we can track the metal enrichment, transportation and dilution throughout the modeled galaxies. We model a massive elliptical galaxy with velocity dispersion ~ 280 km/s, retrieve the chemical composition of the BAL winds launched by the central AGN, and also synthesize the X-ray features of the hot ISM, e.g. the iron abundance seen in thermal X-ray. We find that (1) the simulated metallicity in the BAL winds could be up to $\sim 8Z_{\odot}$, while that of the hot ISM in the host galaxies is $\sim 2.3Z_{\odot}$, matching well with SDSS observations of BLR gas; (2) the X-ray emitting hot gas is metal enriched with a typical value $\sim 2.5Z_{\odot}$; (3) the circumnuclear cold gas disk, where the metals are condensed, further enriched and recycled, plays a critical role in the chemical evolution of its host galaxy (4) the black hole accretion rate \dot{M}_{BH} linearly correlates with the star formation rate \dot{M}_{\star}^{+} in the circumnuclear disk, i.e. $\dot{M}_{\star}^{+} \sim 7.7\dot{M}_{\text{BH}}$, but lagged in time by roughly 10^6 years. The radiative features of the BAL winds are also discussed in this paper, which are testable by direct observations.

Keywords: black hole physics— galaxies: elliptical and lenticular, cD— galaxies: evolution— ISM: abundances— methods: numerical

1. INTRODUCTION

We have developed the MACER (Massive AGN Controlled Ellipticals Resolved) code over some time as an instrument for exploring the evolution of massive elliptical galaxies at high spatial resolution including a relatively complete set of physical processes. A recent paper (Gan et al. 2018) outlines the details of how rotation, massive dark matter halos, infall of cosmological gas and other features were recently added and tested. With this additional physical infrastructure we discovered features expected in the normal evolution of elliptical galaxies that surprised us but for which there is ample observational evidence: specifically the formation of circumnuclear cold gaseous discs that are Toomre unstable and which form massive stars in episodic bursts that fuel the central black hole and explain the enigmatic “E+A” phenomenon. The code, with resolution of parsecs in the central region, resolves the fiducial Bondi radius and hence can treat black hole accretion and AGN (Active Galactic Nucleus) feedback in some detail including both radiative (UV & X-ray) and BAL (Broad Absorption Line) winds in a fashion that imitates the observed output of black holes in both their low and high output states.

In this introductory paper we describe how we can add 12 chemical species produced by standard stellar physics and injected into the interstellar medium (ISM) by asymptotic branch stars (AGBs), type I and type II supernovae (SNe I, SNe II). This will enable us to address a whole new range of questions. For example, “What is the chemical composition expected of the BAL winds?” or “What iron abundance should be seen in the hot X-ray emitting gas?”. These are

questions that most cosmologically based galaxy evolution codes would have difficulty addressing because they typically do not have the spatial resolution needed to resolve the central regions where the winds are generated and a significant part of the new metals are produced.

Half of the observed elliptical galaxies are known to contain cold gaseous discs in their centers (a.k.a circumnuclear disks, e.g., Sarzi et al. 2006; Davis et al. 2011; Boizelle et al. 2017). As we demonstrated in Gan et al. (2018), the formation of circumnuclear disk is inevitable due to the angular momentum barrier, as rotation is the general case. Since the length scale of an AGN is very small when compared to the galactic scale, most of the infalling gas (due to radiative cooling) will settle in a flat, rotationally supported disk-like structure before it reaches the galaxy center (see also Eisenreich et al. 2017). Moreover, the gas will cool down further in the circumnuclear disk, which makes it ideal for star formation.

As cold gas condenses and accumulates on the circumnuclear disk, such a cold gaseous disk would become highly over-dense, and we found that some of the over-dense disk rings would be gravitationally unstable (a.k.a. the Toomre Instability; Toomre 1964; Tan & Blackman 2005). Consequently, angular momentum transfer and star formation are allowed at the same time due to the Toomre instability (e.g., Gammie 2001; Goodman 2003; Rice et al. 2005; Thompson et al. 2005; Machida et al. 2010). Therefore, one may expect a near coincidence of star formation and AGN activity — the former is an important metal enriching source (by SNe II; Goodman & Tan 2004), and via accretion onto the super-massive black hole from the circumnuclear disk and then the

AGN wind feedback, some of the metal enriched gas will be recycled in form of BAL winds — in this paper, we will also demonstrate the key role of the circumnuclear disks in the chemical evolution of massive elliptical galaxies, i.e., where the metals are condensed, further enriched and recycled.

In the next section of this paper we will provide the details of how we implement the chemical abundance inputs to the code. We outline briefly in §3 the model improvements we have made to facilitate the introduction of diverse metallicity components. In §4 we will present some results of computations, including the chemical distribution in the modeled galaxy, the radiative features of the metal rich gas, composition expected in the BAL winds. Conclusions are reserved for final sections.

2. CHEMICAL ABUNDANCES

In the MACER simulations, we solve the continuity equation of the ISM, together with the conservation laws of momentum and energy, including source terms due to the stellar evolution of AGBs ($\dot{\rho}_*$), SNe Ia ($\dot{\rho}_I$) and SNe II ($\dot{\rho}_{II}$) (Ciotti & Ostriker 1997; Novak et al. 2011; Gan et al. 2018), i.e.,

$$\frac{\partial \rho}{\partial t} + \nabla \cdot (\rho \mathbf{v}) + \nabla \cdot \dot{\mathbf{m}}_Q = \dot{\rho}_* + \dot{\rho}_I + \dot{\rho}_{II} - \dot{\rho}_*^+, \quad (1)$$

where ρ and \mathbf{v} are the mass density and fluid velocity, respectively. $\nabla \cdot \dot{\mathbf{m}}_Q$ and $\dot{\rho}_*^+$ are the mass advection due to the Toomre instability (Toomre 1964) and the mass sink term due to star formation, respectively. We refer to our code paper (Gan et al. 2018 and references therein) for the full description of the physics and equations we solve in the simulations.

In this paper, we intend to track the chemical evolution of the metals by using 12 tracers X_i ($i=1, 2, \dots, 12$; mass of each element per unit volume) for H, He, C, N, O, Ne, Mg, Si, S, Ca, Fe and Ni, respectively (see also Eisenreich et al. 2017, Choi et al. 2017 for large scale simulations using SPH). We solve 12 additional continuity equations of the tracers, assuming the chemical species co-move once after they are injected into the ISM, i.e.,

$$\frac{\partial X_i}{\partial t} + \nabla \cdot (X_i \mathbf{v}) + \nabla \cdot \dot{\mathbf{m}}_{Q,i} = \dot{X}_{*,i} + \dot{X}_{I,i} + \dot{X}_{II,i} - \dot{X}_{*,i}^+, \quad (2)$$

where

$$\dot{\mathbf{m}}_{Q,i} = (X_i/\rho) \cdot \dot{\mathbf{m}}_Q, \quad \dot{X}_{*,i}^+ = (X_i/\rho) \cdot \dot{\rho}_*^+, \quad (3)$$

and \mathbf{v} is obtained by solving the hydrodynamical equations as usual. In Equation 2, the passive stellar evolution, i.e., AGBs ($\dot{X}_{*,i}$), SNe Ia ($\dot{X}_{I,i}$) and SNe II ($\dot{X}_{II,i}$), serves as metal-enriching sources, while with different metal compositions (see Table 1). The advection terms $\nabla \cdot (X_i \mathbf{v})$ and $\nabla \cdot \dot{\mathbf{m}}_{Q,i}$ describe the transport and the mixing of ISM with different metal abundances. Star formation ($\dot{X}_{*,i}^+$) is treated as a sink of local metals, but not to change the local abundance.

We start the simulations with an initial stellar population of an age of 2 Gyr, its mass distribution is determined by a galaxy dynamics model (Gan et al. 2018). As cooling flows develop, a circumnuclear disk forms naturally in the galaxy center, in which the gas is cold and over-dense. Star formation is then inevitable. Therefore, we have two stellar populations in our modeled galaxy: (1) the initial stellar population which is 2 Gyr old at the beginning of the simulation, and in which all massive stars have died, while its secular evolution (i.e., AGBs and SNe Ia) is considered in our model. (2) a new

Table 1
Mass fraction of the elements from various sources

	AGBs ^a	SNe Ia ^b	SNe II ^c	CGM ^d	Solar ^e
H	0.71287	0.00000	0.51800	0.74682	0.73810
He	0.26702	0.00000	0.33483	0.25117	0.24850
C	0.00294	0.00225	0.01031	0.00036	0.00241
N	0.00183	0.00000	0.00362	0.00011	0.00071
O	0.00872	0.07465	0.08175	0.00087	0.00585
Ne	0.00190	0.00264	0.02518	0.00019	0.00127
Mg	0.00106	0.01123	0.00761	0.00011	0.00071
Si	0.00047	0.21212	0.00391	0.00010	0.00068
S	0.00101	0.08500	0.00861	0.00005	0.00031
Ca	0.00010	0.01086	0.00050	0.00001	0.00007
Fe	0.00197	0.54693	0.00540	0.00020	0.00132
Ni	0.00011	0.05432	0.00028	0.00001	0.00007
Z	0.0201	1.0000	0.1472	0.0020	0.0134

^a averaged metal abundance of AGB winds over the time span from $t_{\text{age}} = 2$ to 13.7 Gyr, i.e., ($\langle \dot{X}_{*,i}/\dot{\rho}_* \rangle$) (Karakas 2010);

^b metal abundance of SNe Ia ejecta, i.e., ($\dot{X}_{I,i}/\dot{\rho}_I$) (Seitenzahl et al. 2013);

^c metal abundance of SNe II ejecta, i.e., ($\dot{X}_{II,i}/\dot{\rho}_{II}$) (Nomoto et al. 2013);

^d metal abundance of the low-metallicity infalling CGM which is made of 1/4 of primordial gas and 3/4 low metallicity gas of 0.2 solar abundance;

^e solar abundance (Asplund et al. 2009);

^f metallicity Z, i.e., mass fraction of all chemical species except H and He.

stellar population actively forming in the central cold gas circumnuclear disk during the simulations and producing SNe II that plays an important role in the metal enrichment.

We calculate time-dependent nucleosynthesis output returned to the ISM by evolving stars of a simple stellar population (SSP) with “CELlib”, an open-source software library for chemical evolution (Saitoh 2017).

For the initial stellar population, we assume a SSP that consists of stars of identical age and chemical composition, and follows the Kroupa (2001) initial mass function (IMF) with a stellar mass range of $0.1 - 120 M_\odot$. The SSP is assumed of metallicity $Z = 1.5 Z_\odot$ (where $Z_\odot = 0.0134$ is the solar metallicity as quoted in Table 1). This abundance matches that expected for an elliptical as massive as the modeled one, which should be supersolar (e.g., Thomas et al. 2010). The metallicity-dependent stellar lifetime is taken from Portinari et al. (1998). The stellar “yields”, the amount of newly synthesized and ejected elements via stellar evolution, are adopted from Nomoto et al. (2013), Doherty et al. (2014) and Karakas (2010) for high mass stars (Type II SNe), massive AGB stars with $M > 6 M_\odot$, and low mass AGB stars respectively. Our time-dependent chemical enrichment calculation shows that the nucleosynthesis output enriches the ISM mainly via two phases, an early ($t \lesssim 10$ Myr) phase driven by Type II SNe, and a subsequent late phase ($t \gtrsim 40$ Myr) driven by AGB stars (cf. Equation 5). Since our simulation starts at $t_{\text{age}} = 2$ Gyr, there will be only AGBs, and its time-dependent abundance is used in our model as shown in Figure 1, while the averaged metal abundance of AGB winds is also summarized in Table 1 for the readers’ reference.

The initial stellar population also contributes metals via Type Ia SNe (cf. Equation 6). The nucleosynthesis yields of SNe Ia is adopted from Seitenzahl et al. (2013). We have $1.35 M_\odot$ ejecta in total for each SNIa explosion, and the amount of elements distributed by each explosion is adopted from the N100 model of Seitenzahl et al. (2013). For example, as shown in Table 1, the bulk of the $1.35 M_\odot$ ejecta is in Fe ($\sim 0.74 M_\odot$), and some is in Oxygen ($\sim 0.1 M_\odot$) and Silicon

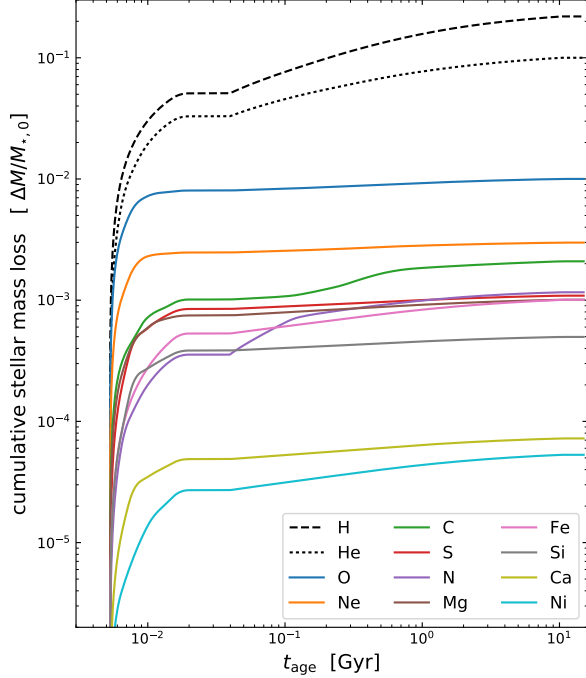


Figure 1. Cumulative mass loss from the initial stellar population in individual chemical species. The lines in colors are the mass fractions of the metals ejected during the passive stellar evolution. The mass losses are in units of $M_{\star,0}$ (i.e., the total mass of the initial stellar population at $t_{\text{age}} = 0$).

($\sim 0.29 M_{\odot}$).

The new stellar population contribute metals, unlike the initial stellar population, mostly in its early phase evolution via massive stars. For simplicity, we only consider the metals ejected by Type II SNe. For such new stellar population formed by gravitational instability in Toomre unstable circumnuclear disks, we adopt the Kroupa IMF, but with the top-heavy index of 1.65 advocated by Bartko et al. (2010) and Lu et al. (2013), which is based on the observed stellar disks in the MW and M31. We adopt a stellar mass range of $1 - 50 M_{\odot}$ (cf. Equation 7). The time-averaged metal abundance of its SN II phase is summarized in Table 1.

As in Gan et al. (2018), we also consider the cosmic accretion (i.e., CGM infall) of low-metallicity gas (cf. Table 1) through the galaxy outskirts, which will dilute the metallicity as it falls into the galaxy and mixes with the ISM there. In addition, we also recycle the metals via the BAL winds which are injected back to the galaxy by the central AGN. Those two processes do not appear explicitly in the equations above, but are implemented via the designed outer and inner boundary conditions, respectively. In this way, we can track the chemical evolution, i.e., the metal enrichment, transportation and dilution, throughout massive elliptical galaxies. After AGN bursts there are significant mass outflows from the galaxy.

To evaluate the metal abundance of the BAL winds, we keep tracking the chemical composition in our AGN “sub-grid” model (Ciotti & Ostriker 1997; Gan et al. 2018). As the mass source of the AGN fueling is accreted via the inner boundary, we record all the metals that pass through to the galaxy center, so that we are able to calculate the averaged metal abundance of the black hole accretion disk at any given time. The BAL winds are injected (at the inner edge) back to the galaxy with the instantaneous metal abundance of the black hole accretion disk.

Finally, we assume the initial ISM is of the solar abundance (Asplund et al. 2009). We must emphasize that we have not yet corrected for the depletion of metals onto dust, and thus our characterization of element abundance is the total (dust plus gas phase) mass in that element per unit volume in units of the local mass density. Especially in the cold gas component, the fractional depletion of refractory elements onto dust grains may be a large correction (Hensley et al. 2014). We reserve it to our future work.

3. MODEL IMPROVEMENTS

Compared to Gan et al. (2018), the model setups have been modified as follows (besides adding the metal tracers) to facilitate the metallicity changes, to improve the model self-consistency, and to better fit the observed galaxy properties:

I. the initial black hole mass is increased by a factor of 2 (i.e., to $M_{\text{BH}} = 6.7 \times 10^8 M_{\odot}$) so as to better match the observed $M_{\text{BH}} - \sigma$ relation (Kormendy & Ho 2013; Yuan et al. 2018), while the rest of the galaxy model parameters are the same as in Gan et al. (2018), i.e., total stellar mass at the present time $M_{\star} = 3.35 \times 10^{11} M_{\odot}$, the effective radius $R_e = 7$ kpc, the galaxy ellipticity $\eta = 0.2$, and the dimensionless parameters for the total gravity mass $\mathcal{R} = 20$ and for the length scale $\xi = 20$ of the modeled galaxy, which results in a central projected stellar velocity dispersion of ~ 280 km/s.

II. in order to describe the ordered rotational velocity of the stellar component we adopted the usual Satoh decomposition in our previous papers, with a constant rotation parameter k (Ciotti et al. 2017; Yoon et al. 2018; Gan et al. 2018). Here we add some flexibility to the modeling by considering a central value (k_0) for the k parameter, and we reduce it in the outer parts of the galaxy as

$$k = k_0 \cdot e^{-r/R_e}, \quad (4)$$

where we adopt $k_0 = 0.25$. In this way we can have some control over the amount of angular momentum stored in the external regions of the galaxy.

III. we adopt the stellar (AGB) mass loss formula in Pellegrini (2012) and adopt the coefficient $A = 3.3$ to match the assumption of the Kroupa IMF, i.e.,

$$\dot{M}_{\star} = 10^{-12} A \cdot \frac{M_{\star}}{M_{\odot}} \left(\frac{t_{\text{age}}}{12 \text{ Gyr}} \right)^{-1.3} M_{\odot}/\text{year}, \quad (5)$$

where t_{age} is the age of the initial stellar population, and the fitting formula is valid when $t_{\text{age}} \geq 2$ Gyr. As usual, the SN Ia rate is evaluated as

$$R_{\text{SN}} = 0.16 \times 10^{-12} h^2 \frac{L_{\text{B}}}{L_{\odot}} \left(\frac{t_{\text{age}}}{12 \text{ Gyr}} \right)^{-1.1} \text{ year}^{-1}, \quad (6)$$

where h is the Hubble constant in units of $70 \text{ km s}^{-1} \text{ Mpc}^{-1}$, and the B-band luminosity L_{B} is derived by adopting a mass-to-light ratio $\Gamma \equiv M_{\star}/L_{\text{B}} = 5.8$ in units of the solar value, as appropriate for an old stellar population with a Kroupa IMF (Pellegrini 2012).

VI. the initial mass function of the newly formed stars in the Toomre unstable disks is assumed to have a top-heavy profile based on both observations and theoretical expectations (Goodman & Tan 2004; Bartko et al. 2010; Jiang & Goodman 2011; Lu et al. 2013), we assume

$$\frac{dN}{dM} = \frac{N_0}{M_{\odot}} \left(\frac{M}{M_{\odot}} \right)^{-1.65} \quad (7)$$

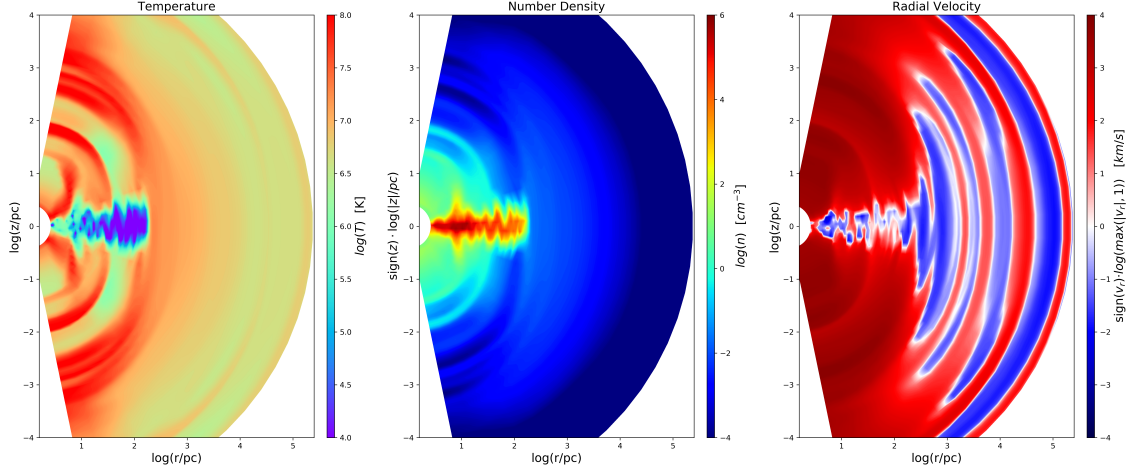


Figure 2. Hydrodynamical properties of the ISM during the burst event at $t_{\text{age}} = 12.1$ Gyr. The size of the cold gaseous disk is ~ 150 parsec. The high-speed BAL winds is of a bi-conical structure and can be heated up to 10^8 K. Note the logarithmic radial scale.

with a mass range of $1 - 50 M_{\odot}$. Such an IMF gives that $\sim 60\%$ of the total new star mass is in massive stars ($M > 8 M_{\odot}$), which will turn into SNe II in a timescale of $\sim 2 \times 10^7$ year. We assume each SN II leaves a neutron star of $1.4 M_{\odot}$ and ejects 10^{51} erg of energy into the ISM (cf. Ciotti & Ostriker 2012).

V. we allow for the fact that the atomic heating/cooling function (S_{line}) is approximately proportional to the local metallicity ($Z \equiv 1 - (X_1 + X_2)/\rho$) in units of the solar value $Z_{\odot} = 0.0134$, i.e., in the net heating rate $H - C = n^2(S_{\text{comp}} + S_{\text{brem}} + S_{\text{line}})$,

$$S_{\text{line}} = 10^{-23} \frac{a + b(\xi/\xi_0)^c}{1 + (\xi/\xi_0)^c} \frac{Z}{Z_{\odot}}, \quad (8)$$

S_{comp} and S_{brem} are as usual the Compton heating/cooling and the bremsstrahlung loss, respectively (detailed description of the heating/cooling functions above can be found in Ciotti & Ostriker 2012).

VI. we use the same CGM infall profile as in Gan et al. (2018), however, since we start the simulation when the galaxy is 2 Gyr old, we now also start the CGM infall at that time. The accumulated mass due to the CGM infall before $t_{\text{age}} = 2$ Gyr is now taken as the initial remnant ISM, which is $\sim 10^{10} M_{\odot}$.

VII. the AGN feedback wind efficiency ϵ_w is reduced from 0.005 to 0.004.

Finally, we solve the ISM hydrodynamical equations, together with the metal tracers, using the grid-based Athena++ code (version 1.0.0; Stone et al. 2008) in spherical coordinates. We assume axi-symmetry but allow rotation (a.k.a. 2.5-dimensional simulation). The outer boundary is chosen as 250 kilo-parsec to enclose the whole massive elliptical galaxy, the inner boundary R_{in} is set to be 2.5 parsec to resolve the Bondi radius. We use a logarithmic grid ($\Delta r_{i+1}/\Delta r_i = 1.1$) to divide the radial axis into 120 discrete cells. The azimuthal angle θ is divided into 30 uniform cells and covers an azimuthal range from 0.05π to 0.95π . The numerical solver for the gas dynamics is composed by the combination of the HLLC Riemann Solver, the PLM reconstruction and the second-order van Leer integrator.

4. RESULTS

Before we address the simulation details, it is helpful to discuss the “closed-box problem”, i.e., what metal composition

could be expected if the metal enrichment is only contributed by the secular evolution of the initial old stellar population, i.e., via AGBs and SNe Ia? We can see from Figure 1 that the metal composition of AGB winds provides only weak evolution after $t_{\text{age}} = 2$ Gyr (when the simulation starts), and we use a fixed metal composition for SN Ia ejecta. Moreover, Equations 5 & 6 give that the ratio between the mass return rates of SNe Ia and AGBs evolves weakly from 0.008 to 0.012. Therefore, the secular stellar evolution (AGBs + SNe Ia) alone will result in a characteristic metallicity in a narrow range of $2.1 Z_{\odot} < Z < 2.4 Z_{\odot}$ throughout the host galaxy.

In addition, as mentioned in §2, SNe II contribute to the metal enrichment when there is star formation, while star formation mainly occurs in the circumnuclear disk, where most of the infalling gas is circularized because of angular momentum barrier. Ideally, local metallicity could be up to $12.7 Z_{\odot}$ if SNe II dominate the metal enrichment (cf Table 1).

We will demonstrate in the rest of this section that the metal enrichment in the circumnuclear disk is the key to understanding the chemical evolution of the modeled galaxy. Therefore, it is worthwhile to analyze the circumnuclear disk in advance (see §4.1). Following the physical sequence, i.e., formation of the circumnuclear disk, star formation, mass inflow, BAL winds, and then metal transportation, we perform in §4.2 detailed analysis on the star formation and black hole feeding processes. In §4.3, we present the overall gaseous mass and metal budget. In §4.4, the spatial distribution of metals is presented, and we will see the role of the BAL winds in transporting metals throughout the modeled galaxy. Finally, the radiative features of the metal-enriched hot ISM are calculated in §4.5.

4.1. Circumnuclear disk

In Figure 2, we present the hydrodynamical properties of the ISM during the burst event at $t_{\text{age}} = 12.1$ Gyr. The gaseous counterpart of the circumnuclear disk is found of a size ~ 150 parsec, and of mass $\sim 2.5 \times 10^8 M_{\odot}$ (see Figure 3 for the stellar counterpart). It is shown in the polar regions that the high-speed BAL winds launched by the central AGN can be heated up to 10^8 K, which should be capable in emitting X rays. We have designated as BAL wind gas flowing out of the galaxy center with radial velocity ≥ 1000 km/s. Also, metal-rich gas, recycled from circumnuclear disk, will be transported through the galaxy by virtue of the high-speed

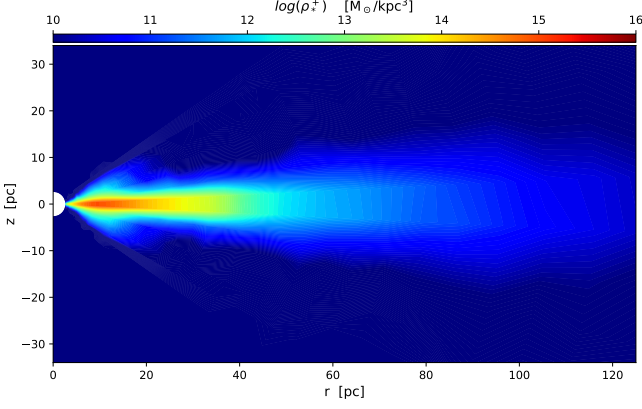


Figure 3. Cumulative star formation in the circumnuclear disk at $t_{\text{age}} = 12.1$ Gyr. The size of the stellar disk is < 150 parsec. The cumulative star formation in the disk is $\sim 6.5 \times 10^9 M_{\odot}$. The averaged age and metallicity of the new stellar population are 7.52 Gyr and $Z/Z_{\odot} = 5.82$, respectively.

BAL winds.

In Figure 3, we show the cumulative star formation in the circumnuclear disk, which is $\sim 6.5 \times 10^9 M_{\odot}$ at $t_{\text{age}} = 12.1$ Gyr. The stellar disk of the newly formed stars is of a thin geometry, and its size is $\lesssim 150$ parsec, which coincides with the cold gaseous disk (cf. Figure 2). Recall that we have two star formation algorithms in our model setup: one is based on the Toomre instability and the second on the local Jeans timescale, with the latter allowed only in the densest gaseous zones with hydrogen number density $n_H > 10^5 \text{ cm}^{-3}$ (Gan et al. 2018). So, most of the star formation is confined to the innermost region of the circumnuclear disk. In the simulation, we are able to track the age and the in-situ metallicity of the newly formed stars, as shown in Figure 3, the averaged age and metallicity of the new stars are 7.52 Gyr and $Z/Z_{\odot} = 5.82$, respectively.

4.2. Star formation vs. mass accretion

As we discussed previously, it is the Toomre instability that primarily triggers star formation and allows mass inflow simultaneously. So it is unavoidable to expect a coincidence between AGN bursts and star formation (Goodman 2003; Kawakatu & Wada 2008; Imanishi et al. 2011; Diamond-Stanic & Rieke 2012; Esquej et al. 2014; Izumi et al. 2016, 2018). In Figure 4, we plot the history of star formation rate \dot{M}_{\star}^{+} (blue line) and the mass inflow rates (that through the inner boundary \dot{M}_{in} in yellow line, and that onto the black hole horizon \dot{M}_{BH} in green line, respectively). As expected, the AGN activities are usually coincident roughly with star formation, and the instantaneous star formation rate \dot{M}_{\star}^{+} is typically much larger than the mass inflow rate through the inner boundary \dot{M}_{in} (or the black hole accretion rate \dot{M}_{BH}). That is, star formation consumes most of the cold gas within the circumnuclear disk before it can fall onto the central supermassive black hole. This also means that SNe II in the new stellar population can play a very important role in enriching metals (see §4.3 for detailed analysis).

In Figure 5, we present the scatter plot between the black hole accretion rate \dot{M}_{BH} and star formation rate \dot{M}_{\star}^{+} , where we bin the timing data in Figure 4 with adjacent time intervals of $\Delta t = 10^6$ and 10^7 year, respectively, as shown with the blue (open) and yellow (filled) cycles. We find a tight linear correlation of $\dot{M}_{\star}^{+} \sim 7.7 \dot{M}_{\text{BH}}$. Note that no correlation can be found before binning the data, due to the time lags between

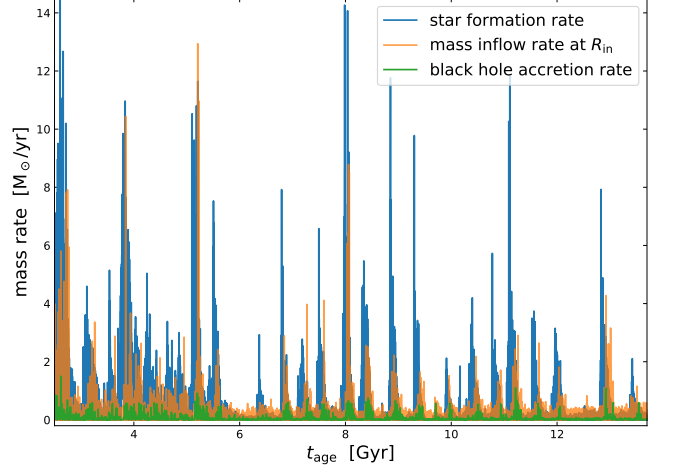


Figure 4. History of the star formation and AGN activities. The blue, green, and orange lines show the variations of the star formation rate, mass inflow rate onto the galaxy center through the inner boundary (R_{in}), and the black hole accretion rate, respectively. As shown in the figure, black hole accretion events usually associate with star formation.

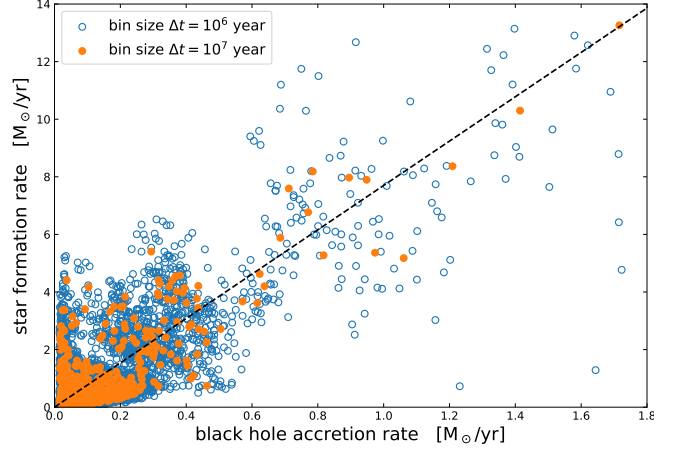


Figure 5. The scatter plot between the black hole accretion rate \dot{M}_{BH} and star formation rate \dot{M}_{\star}^{+} . In the figure, we bin the timing data in Figure 4 with adjacent time intervals of $\Delta t = 10^6$ and 10^7 year, respectively, as shown with the blue (open) and yellow (filled) cycles. We find a tight correlation of $\dot{M}_{\star}^{+} \sim 7.7 \dot{M}_{\text{BH}}$. Note that no correlation can be found before binning the data, due to the time lags between star formation and black hole accretion.

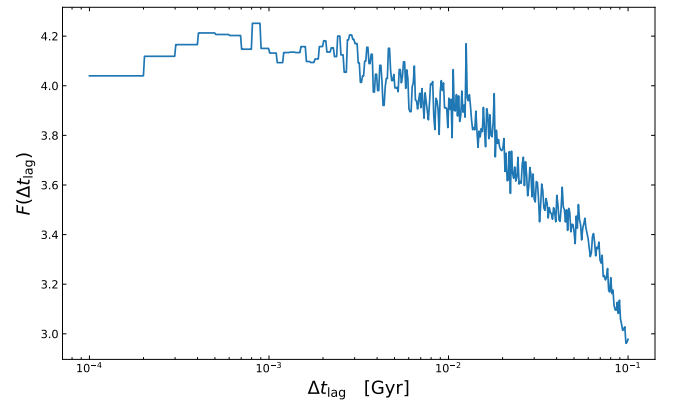


Figure 6. The time lag between star formation and black hole accretion (cf Equation 9).

star formation and black hole accretion. To evaluate the time lags, we perform the calculation below,

$$F(\Delta t_{\text{lag}}) = \frac{\int \dot{M}_{\star}^{+}(t) \cdot \dot{M}_{\text{BH}}(t + \Delta t_{\text{lag}}) dt/T}{\int \dot{M}_{\star}^{+}(t) dt/T \cdot \int \dot{M}_{\text{BH}}(t) dt/T} \quad (9)$$

where $T = 12$ Gyr is the duration of the simulation. The results are shown in Figure 6. It indicates that the time lag between star formation and black hole accretion is about few 10^6 year.

4.3. Overall chemical budget

The cumulative chemical yields from the initial (old) stellar population and the new (young) stellar population are shown in Figure 7 with the solid and dashed lines, respectively. During the simulation, the old stellar population ejects in total $\sim 3.4 \times 10^{10} M_{\odot}$ of total mass into the ISM ($\sim 10\% M_{\star}$; cf Equations 5 & 6). The cumulative star formation is $\sim 6.7 \times 10^9 M_{\odot}$ in total, of which 58% is injected into the ISM via SNe II (cf Equation 7), i.e., the new stellar population contributes $\sim 1/10$ of the total stellar mass loss (see the black lines in the top panel), while it dominates the chemical yields of Neon and contributes significantly to Oxygen as shown in the middle panel. The new stellar population also contributes a significant fraction of heavy metals when compared to that of the initial stellar population as shown in the bottom panel. Note that star formation mainly occurs in the circumnuclear disk.

With the metal sources and the flow pattern as described above, we are ready to analyze the metal enrichment and its transportation throughout the modeled galaxy. As shown in Table 1, SN II ejecta is enriched in alpha elements (especially Ne and O); SN Ia ejecta is of the highest mass fraction of Fe and Si; AGBs produce a relatively high fraction of Nitrogen. So it is possible for us to track the stellar evolution by using the elements mentioned above.

4.4. Spatial distribution of metals

In Figure 8, we present the spatial distribution of the metallicity Z and individual chemical species (Fe, Ne, C, O, S) during the burst event at $t_{\text{age}} = 12.1$ Gyr. We find that the characteristic metal abundances are different from place to place, accordingly, the modeled galaxy can be divided into three parts: (1) the circumnuclear disk, i.e., ($r = 0.10$ kpc, $\theta = \pi/2$) and the surrounding region; (2) the BAL region, i.e., ($r = 0.05$ kpc, $\theta \leq \pi/6$); (3) the main body of the galaxy on the length scale of 10 kpc, i.e., ($r = 10$ kpc, $\theta = \pi/2$). We sample the metal abundances from the representative locations above and show the results in Table 2. The high metallicities found in the BAL region and in the cold disk are consistent with the SDSS observations (e.g., Nagao et al. 2006; Xu et al. 2018).

As shown in top-middle panel of Figure 8, the main body of the galaxy shows the highest Fe abundance (e.g. at $r \sim 10$ kpc, $\theta = \pi/2$). As we discussed previously, the secular stellar evolution of the old stellar population dominates the metal enrichment since there is no star formation in the main body of the galaxy. The typical value of the metallicity Z is $\sim 2.3 Z_{\odot}$, and it follows the abundance pattern of AGBs + SNe Ia (cf. Table 2) as discussed at the beginning of this section.

As shown in top-left panel of Figure 8, the circumnuclear disk has the highest metallicity, with a typical value up to $\sim 8 Z_{\odot}$ in the innermost region and decreasing to $\sim 2.3 Z_{\odot}$ at its outer edge. Obviously, SNe II play a crucial role in the

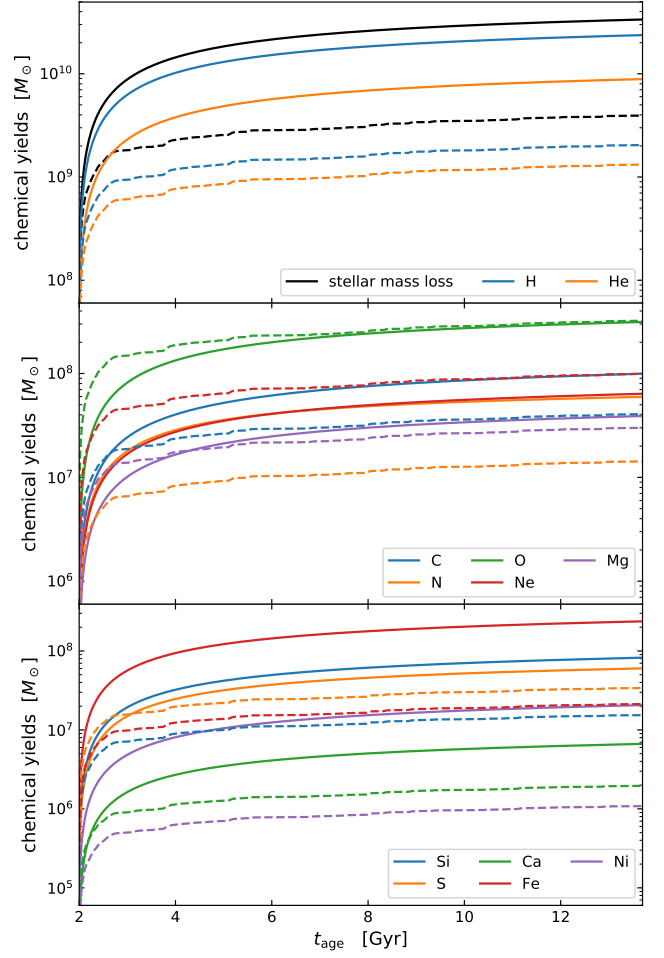


Figure 7. Cumulative chemical yields from the initial (old) stellar population (solid lines) and the new stellar population (dashed lines). The black lines in the top panel present the cumulative stellar mass loss from the two stellar populations, respectively, i.e., the new stellar population (black dashed line) contributes $\sim 1/10$ of the total mass loss, while it dominates the chemical yields of Neon and contributes significantly to Oxygen (middle panel). The new stellar population also contributes a significant fraction of heavy metals when compared to that of the initial stellar population (bottom panel).

Table 2
Metal abundance of sampled interstellar medium*

	hot ISM	cold disk	BAL region
He/H	1.11	1.23	1.44
C/H	1.40	2.04	3.20
N/H	2.19	2.46	2.96
O/H	1.76	5.68	12.8
Ne/H	1.62	6.49	15.4
Mg/H	1.79	4.18	8.55
Si/H	4.36	5.11	6.56
S/H	6.51	12.7	23.9
Ca/H	3.48	4.94	7.64
Fe/H	6.32	6.03	5.60
Ni/H	10.3	9.07	7.00
Z/Z_{\odot}	2.34	4.54	7.96

* The metal abundances are sampled at $t_{\text{age}} = 12.1$ Gyr from the hot ISM ($r = 10$ kpc, $\theta = \pi/2$), the cold circumnuclear disk ($r = 0.10$ kpc, $\theta = \pi/2$), and the BAL region ($r = 0.05$ kpc, $\theta = \pi/6$), respectively. All the measurements are in the solar units as defined in Table 1.

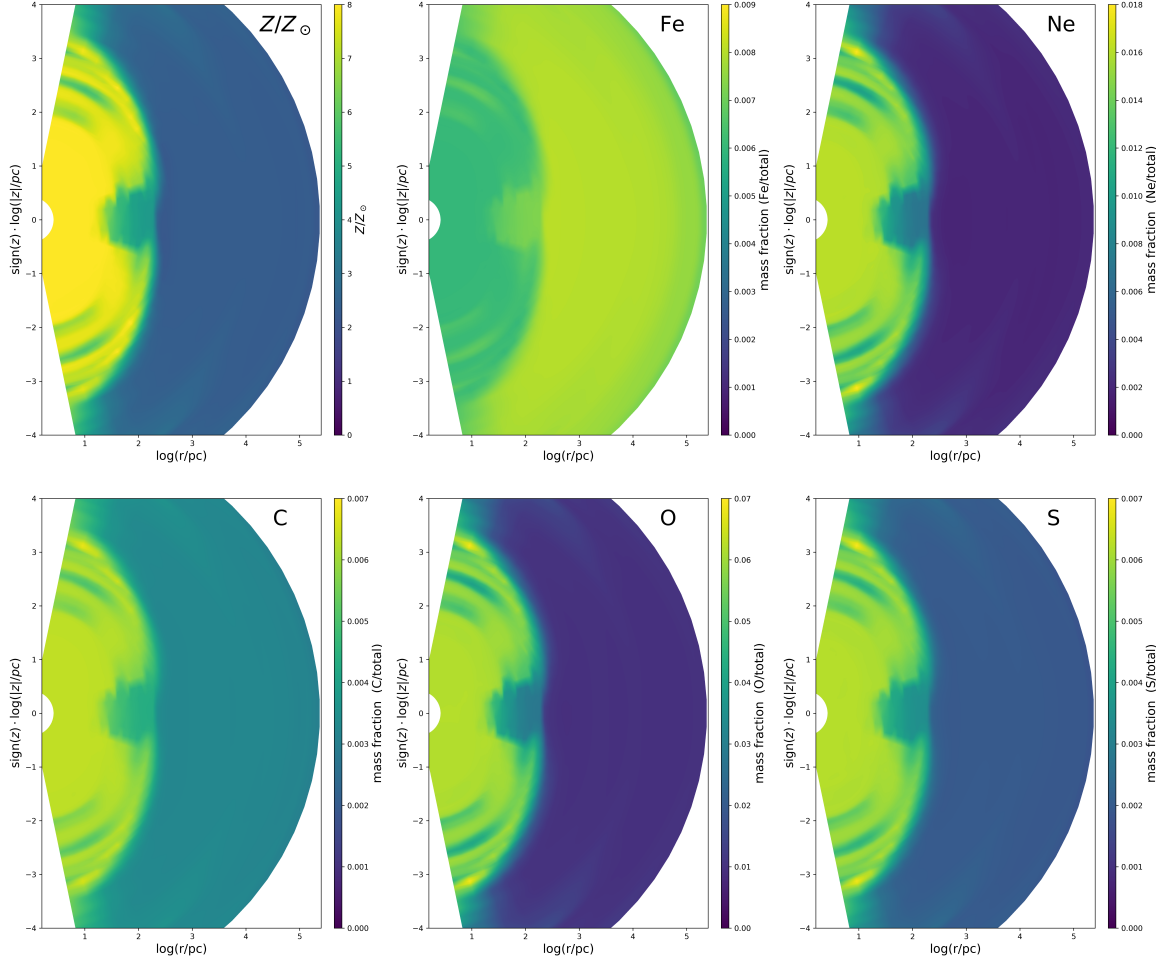


Figure 8. Spatial distribution of the metallicity Z and individual chemical species (Fe, Ne, C, O, S) during the burst event at $t_{\text{age}} = 12.1$ Gyr. The metallicity Z is in units of the solar value ($Z_{\odot} = 0.0134$), and reaches a maximum value $8.04Z_{\odot}$ and on average (mass-weighted) of $3.96Z_{\odot}$ in the BAL winds. For the selected chemical species, the mass fractions with respect to the total local gas mass are shown in the bottom panels. Note the logarithmic radial scale.

metal enrichment within the circumnuclear disk. Note that the disk here seems much more puffy than its geometry seen in the hydrodynamical counterpart (cf Figure 2), which is because the massive SN II explosions contaminate the chemical composition above and below the disk. We use Neon to track the contributions of SNe II to the metal enrichment in the upper-right panel, we can see that the spatial distribution of Neon follows well with the biconical structure of the BAL winds (cf Figure 2; alpha elements shown in the bottom panels of Figure 8 also share the similar patterns). As we mentioned, the AGN feeding process is mainly via the circumnuclear disk. Therefore, the BAL winds would naturally inherit the high metallicity of the circumnuclear disk, and spread the metal-rich gas in a fashion of biconical winds. The metallicity of the BAL winds is up to $\sim 8Z_{\odot}$ and on average (mass-weighted) it is $\sim 3.96Z_{\odot}$, because it is diluted by the ISM while the wind is propagating through its host galaxy. Detailed metal composition of the BAL winds (during three representative burst events, at $t_{\text{age}} = 4.0, 8.1, 12.1$ Gyr, respectively) can be found in Table 3, as previously, we define the BAL winds as the components moving with radial velocity ≥ 1000 km/s.

We also see at the early epochs that the galaxy outskirts has extremely low metallicity because of the dilution due to the low-metallicity CGM infall (not shown here). When such gas

cools down and falls onto the galaxy, it would also dilute the metal abundance in the circumnuclear disk.

Table 3
Mass-weighted metal abundance in the BAL winds*

	Peak 1 ($t_{\text{age}} = 4.0$ Gyr)	Peak 2 ($t_{\text{age}} = 8.1$ Gyr)	Peak 3 ($t_{\text{age}} = 12.1$ Gyr)
He/H	1.17	1.22	1.20
C/H	1.64	1.94	1.88
N/H	2.85	2.57	2.39
O/H	3.91	5.23	4.66
Ne/H	4.33	5.95	5.20
Mg/H	3.08	3.89	3.58
Si/H	4.16	4.83	4.95
S/H	9.47	11.8	11.1
Ca/H	3.99	4.69	4.59
Fe/H	5.33	5.80	6.15
Ni/H	8.06	8.68	9.48
Z/Z_{\odot}	3.50	4.25	3.96

* The measurements are made in the BAL regions which are selected if radial velocity $v_r \geq 1000$ km/s. The metal fractions are weighted by the total ISM mass. Note that the metallicity of the BAL winds is diluted by the ISM while it is propagating through its host galaxy. All the measurements are in the solar units as defined in Table 1.

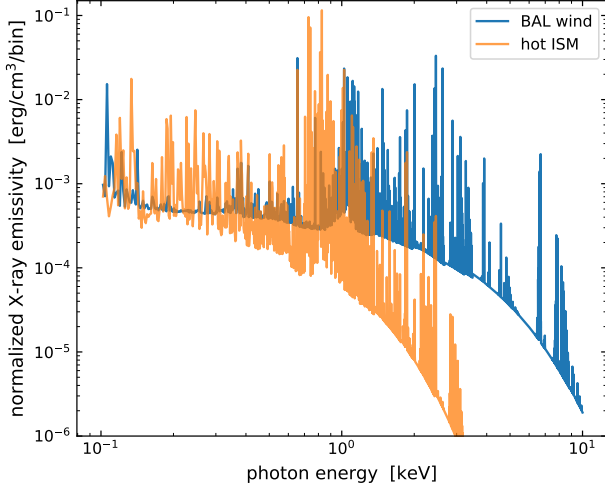


Figure 9. Metallicity-dependent X-ray emissivities with the sampled metal abundances in Table 2. The BAL sample is of a typical temperature $\sim 2 \times 10^7$ K, and that of the hot ISM is $\sim 5 \times 10^6$ K.

4.5. Metals seen in X-rays

As a result of metal enrichment, the radiative cooling and *photoionization* heating of the ISM are significantly enhanced. We pay special attention to finding observable features which can be used to test our model. In the rest of this section, we will perform detailed analysis on the radiative features of the hot ISM, and illustrate the advantages of computing detailed metallicity. The post processing is based on the hydrodynamical data. The frequency-dependent radiation is calculated using the atomic database ATOMDB (version 3.0.9; assuming collisional equilibrium), for example, at any given time and location, we retrieve the ISM properties, i.e., its density, temperature, and the detailed abundance of the 12 chemical species. Then, we take such output from the MACER simulation as the input of ATOMDB, ultimately, the latter would give us the emissivity in the energy band of interest.

In Figure 9, we plot the representative X-ray spectra for the hot ISM and BAL winds as sampled in Table 2. The BAL sample is of a typical temperature $\sim 2 \times 10^7$ K, and that of the hot ISM is $\sim 5 \times 10^6$ K. With the metallicity-dependent emissivity, we are able to synthesize the radiative features of the hot gas.

In the top two panels of Figure 10, we plot the X-ray luminosities and the mass of the hot ISM. We can see that the ISM X-ray luminosity decreases systematically from redshift $z=3.2$ to 0, which is mainly because of the decrease of gas content in the modeled galaxy.

In the lower panels of Figure 10, we analyze the X-ray-emission weighted properties of the hot ISM. We average a quantity of interest P in the manner below,

$$\langle P \rangle \equiv \frac{\int j_\nu P dV}{\int j_\nu dV}. \quad (10)$$

where j_ν is the X-ray emissivity in the energy band of 0.3–8 keV. In the volume integrals above, we exclude the disk region ($r < 200$ parsec and $\pi/3 < \theta < 2/3\pi$) and the densest zones with $n_H > 10^2 \text{ cm}^{-3}$, i.e., which corresponds approximately to a column density of $10^{23} \text{ atom/cm}^2$ and may be optically thick to X-rays (Ballantyne 2008); The X-ray-emission

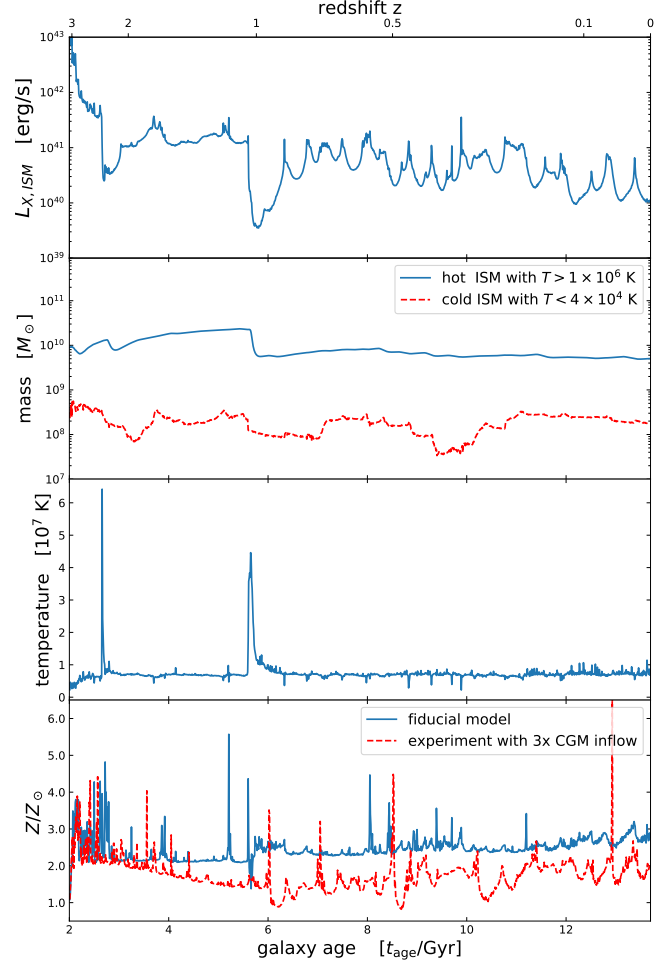


Figure 10. X-ray-emission-related properties of the hot ISM. From top to bottom, it shows the X-ray luminosity, total ISM mass, X-ray-emission weighted temperature and metallicity, respectively. Note that the disk region ($r < 200$ parsec and $\pi/3 < \theta < 2/3\pi$) and the densest zones with hydrogen number density $> 10^2 \text{ cm}^{-3}$ are excluded in the calculations of the X-ray-emission weighted properties above. The red dashed line in the bottom panel shows the X-ray-emission weighted metallicity in an experimental run with three times higher CGM inflows when compared to our fiducial model in this paper.

weighted ISM temperature is presented in the second panel from bottom, the typical temperature is ~ 0.7 keV which is comparable to the virial temperature on the length scale of 10 kpc. The averaged metallicity is shown in the bottom panel, of which the typical value is $\sim 2.5 Z_\odot$, while with Fe abundance approximately $\sim 6 \times$ the solar value.

5. CONCLUSIONS AND DISCUSSIONS

We have developed the MACER code as an instrument for exploring the evolution of massive elliptical galaxies at high spatial resolution down to and within the fiducial Bondi radius, which enables us to evaluate the black hole feeding and feedback processes in a self-consistent way, and to track the coevolution between the supermassive black holes and their host galaxies. In the MACER simulations, we paid special attention to the internal secular stellar evolution which plays a crucial role in driving the galaxy evolution as important sources of mass and energy for the ISM. As an increment to the MACER code, in this paper, we track the recycled mass from the stellar physics with its detailed chemical abundances. Such an increment provides us unprecedented details of the

ISM properties, which are testable by direct comparison with observations.

To trace the metal enrichment, transportation and dilution processes, we solved 12 additional continuity equations dedicated to H, He, C, N, O, Ne, Mg, Si, S, Ca, Fe and Ni respectively. The metal yields, from AGBs and supernovae of type Ia and II, are calculated based on standard stellar physics. The chemical species are assumed to co-move once after they are injected into the ISM, and they are naturally mixed following the fluid motion.

As expected, a Toomre unstable circumnuclear disk forms in the galaxy center with a size of ~ 150 parsec, which plays a crucial role in the chemical evolution of its host galaxy — it is where the metals are condensed, further enriched and recycled. The half mass radius of the new stars is roughly 20 parsec. More specifically, the massive stars formed in the cold gas disk supplement a significant fraction of metals. From Figure 3 we see that of order 10^6 massive stars will be formed over the lifetime of a massive galaxy. In their death throes, they will produce core collapse SNe II spewing out alpha rich chemical products. As a result, the metallicity of the disk in the innermost region reaches up to $\sim 8Z_{\odot}$ (Figure 8). Such metal-rich gas will be captured by the supermassive black hole, and then much of it will be recycled back to its host galaxy by virtue of high-speed BAL winds. The latter can be readily observed. We found that the simulated metallicity in the BAL winds could be up to $\sim 8Z_{\odot}$, while that of its host galaxy is $\sim 2.3Z_{\odot}$. The X-ray emitting hot gas is very metal enriched with a fluctuating value typically near $3Z_{\odot}$.

Our results are well consistent with the clear correlation found observationally between quasar luminosities and their nuclear gas metallicity (Warner et al. 2003; Nagao et al. 2006; Matsuoka et al. 2011; Xu et al. 2018). Xu et al. (2018) analyzed the metallicity of quasar broad line region (BLR) with a large SDSS sample. They found that the metallicity in the most massive galaxies is $\sim 2Z_{\odot}$, while the BLR metallicity is $0.3 \sim 1.0$ dex larger than their host galaxies and it does not evolve with cosmic time. It indicates that the metal enrichment is due to recent star formation rather than secular stellar evolution, as we found in this paper. In the MACER simulation, the spatial resolution is close to the BLR length scale, we also found clear correlation between star formation and AGN bursts (but lagged in time by roughly 10^6 years), and thus significant metal enrichment in the galaxy center. The ratio of star formation in the circumnuclear disk to accretion towards to the central supermassive black hole is 2.3, and of that amount the bulk (62%) is blown out in the BAL winds with a fraction of 38% finally accreted onto the black hole.

Our simulated metallicity, both for the innermost central region and for the main body of the modeled galaxy, is larger than derived from X-ray observations (e.g., see Humphrey & Buote 2006, Mernier et al. 2017 for the abundance of the hot ISM of early-type galaxies). However, there are a number of uncertainties when deriving abundances from the X-ray spectra (see Kim 2012 for a review). Also, dust depletion of metals could be a significant factor (e.g., see Lakhchaura et al. 2018 for a recent analysis). Additionally we assumed a metallicity of $1.5Z_{\odot}$ which seemed reasonable given that the velocity dispersion of our test galaxy is roughly double that in the MW spheroid. However, as noted earlier, Conroy et al. (2014) would give our test galaxy a Fe abundance (in the old stars) slightly less than the solar value.

One important caveat should be noted in our discussion of the expected chemical abundances in the X-ray emitting gas.

We allowed for CGM infall of metal poor gas, but the amount of infall in our fiducial simulation was only $1/12$ of the stellar mass of the initial galaxy, and even somewhat less than that ($\sim 1/20$) when we corrected for starting at 2 Gyr. This could be too low an estimate and, in any case, will vary from case to case depending on the detailed cosmic environment. To check on the sensitivity to this component we have run a case with three times higher CGM inflow ($1/4$ of the initial stellar mass corrected to $\sim 1/7$ of the stellar mass at $t = 2$ Gyr). In this test run the CGM inflow dilutes the metallicity enrichment to such an extent that the final X-ray-emission weighted metallicity drops to ~ 1.5 times solar by roughly a factor of two from our fiducial run. Thus the expected metallicity of the hot X-ray emitting gas has an almost factor of two uncertainty depending on the cosmic environment — an uncertainty that can only be addressed by simulations that are both cosmologically correct and have very high internal spatial resolution.

The massive stars formed in the Toomre unstable central cold gas disk should have dramatic observable consequences, besides the metal enrichment. For example, the SN II going off in the central disk will also produce a copious X-ray output as indicated in Figure 2. However, those SN remnants occur in such dense regions that even the X-ray may not be observable except from the “runaway” star explosions and these are not allowed for in the current simulations.

In addition, the (million) neutron star and black hole condensed remnants of the exploded early type stars must be considered. If they survive in the discs, then accretion onto them should have major consequences and they would be dramatically visible in the “E + A” phases when the gas discs have largely dissipated. But there is another phenomenon which may intervene. The embedded condensed remnants will interact with the dense gas disk and be dragged into the central supermassive black hole in a manner labeled Type I migration first discussed by Goldreich & Tremaine (1980; which is important in planet formation). Using the Equation 70 of Tanaka et al. (2002), we estimate that the migration time is comparable to the Hubble time especially for $10M_{\odot}$ black holes. Using Type I migration underestimates the migration rate since it does not allow for the fact that the discs are so dense that in places they are marginally Toomre unstable. This predictable set of processes would produce high mass ratio black hole captures (a.k.a. “Extreme Mass Ratio Inspiral”, or in short EMRI) which, while undetectable by LIGO, would be candidates for LISA detection (e.g., Babak et al. 2017). A zeroth order estimate of the rate gives $10^{2.5}$ events/year within 1000 mpc.

In this paper, we did not consider the effect of runaway stars in the star-forming circumnuclear disk, which could be important in spreading metals in the galaxy center. We also did not yet consider the dust effects in depleting metals and obscuring radiation, which could alter the radiative features of the circumnuclear disk significantly. In the near future, we will introduce the above effects into the MACER simulations, aiming to interpret/predict the observed/observable radiative features of the “E+A” phenomena.

ACKNOWLEDGEMENT

We thank Kengo Tomida for helping us to add tracers into the Athena++ code. We thank Jeremy Goodman, James Stone, Pieter van Dokkum, Nadia Zakamska, Takayuki Saitoh, Tuguldur Sukhboldfor and Charlie Conroy for useful discussions. ZG is supported in part by the Natural Science Foundation of Shanghai (grant 18ZR1447200) and by

the Chinese Academy of Sciences via the visiting scholar program. This work was done during ZG's visit to the department of astronomy in Columbia University. We acknowledge computing resources from Columbia University's Shared Research Computing Facility project, which is supported by NIH Research Facility Improvement Grant 1G20RR030893-01, and associated funds from the New York State Empire State Development, Division of Science Technology and Innovation (NYSTAR) Contract C090171, both awarded April 15, 2010. Some of the simulations presented were performed with the computing resources made available via the Princeton Institute for Computational Science and Engineering.

REFERENCES

- Asplund, M., Grevesse, N., Sauval, A. J., & Scott, P. 2009, *Annual Review of Astronomy and Astrophysics*, 47, 481
- Babak, S., Gair, J., Sesana, A., et al. 2017, *Physical Review D*, 95, doi:10.1103/PhysRevD.95.103012, arXiv: 1703.09722
- Ballantyne, D. R. 2008, *The Astrophysical Journal*, 685, 787
- Bartko, H., Martins, F., Tripp, S., et al. 2010, *ApJ*, 708, 834
- Boizelle, B. D., Barth, A. J., Darling, J., et al. 2017, *The Astrophysical Journal*, 845, 170
- Choi, E., Ostriker, J. P., Naab, T., et al. 2017, *The Astrophysical Journal*, 844, 31
- Ciotti, L., & Ostriker, J. P. 1997, *The Astrophysical Journal Letters*, 487, L105
- Ciotti, L., & Ostriker, J. P. 2012, in *Hot Interstellar Matter in Elliptical Galaxies, Astrophysics and Space Science Library*, Vol. 378 (eprint: arXiv:1104.2238: Springer Science+Business Media, LLC), 83
- Ciotti, L., Pellegrini, S., Negri, A., & Ostriker, J. P. 2017, *The Astrophysical Journal*, 835, 15
- Conroy, C., Graves, G. J., & Dokkum, P. G. v. 2014, *ApJ*, 780, 33
- Davis, T. A., Alatalo, K., Sarzi, M., et al. 2011, *Monthly Notices of the Royal Astronomical Society*, 417, 882
- Diamond-Stanic, A. M., & Rieke, G. H. 2012, *The Astrophysical Journal*, 746, 168
- Doherty, C. L., Gil-Pons, P., Lau, H. H. B., Lattanzio, J. C., & Siess, L. 2014, *Monthly Notices of the Royal Astronomical Society*, 437, 195
- Eisenreich, M., Naab, T., Choi, E., Ostriker, J. P., & Emsellem, E. 2017, *Monthly Notices of the Royal Astronomical Society*, 468, 751
- Esquej, P., Alonso-Herrero, A., González-Martín, O., et al. 2014, *ApJ*, 780, 86
- Gammie, C. F. 2001, *The Astrophysical Journal*, 553, 174
- Gan, Z., Ciotti, L., Ostriker, J. P., & Yuan, F. 2018, arXiv:1809.04169 [astro-ph], arXiv: 1809.04169
- Goldreich, P., & Tremaine, S. 1980, *The Astrophysical Journal*, 241, 425
- Goodman, J. 2003, *Monthly Notices of the Royal Astronomical Society*, 339, 937
- Goodman, J., & Tan, J. C. 2004, *The Astrophysical Journal*, 608, 108
- Hensley, B. S., Ostriker, J. P., & Ciotti, L. 2014, *The Astrophysical Journal*, 789, 78
- Humphrey, P. J., & Buote, D. A. 2006, *The Astrophysical Journal*, 639, 136
- Imanishi, M., Ichikawa, K., Takeuchi, T., et al. 2011, *Publications of the Astronomical Society of Japan*, 63, 447
- Izumi, T., Kawakatu, N., & Kohno, K. 2016, *ApJ*, 827, 81
- Izumi, T., Wada, K., Fukushige, R., Hamamura, S., & Kohno, K. 2018, *ApJ*, 867, 48
- Jiang, Y.-F., & Goodman, J. 2011, *The Astrophysical Journal*, 730, 45
- Karakas, A. I. 2010, *Monthly Notices of the Royal Astronomical Society*, 403, 1413
- Kawakatu, N., & Wada, K. 2008, *The Astrophysical Journal*, 681, 73
- Kim, D.-W. 2012, in *Hot Interstellar Matter in Elliptical Galaxies*, Vol. 378 (New York, NY: Springer New York), 121
- Kormendy, J., & Ho, L. C. 2013, *Annual Review of Astronomy and Astrophysics*, 51, 511
- Kroupa, P. 2001, *Monthly Notices of the Royal Astronomical Society*, 322, 231
- Lakhchaura, K., Mernier, F., & Werner, N. 2018, arXiv e-prints, 1812, arXiv:1812.00121
- Lu, J. R., Do, T., Ghez, A. M., et al. 2013, *The Astrophysical Journal*, 764, 155
- Machida, M. N., Inutsuka, S.-i., & Matsumoto, T. 2010, *ApJ*, 724, 1006
- Matsuoka, K., Nagao, T., Marconi, A., Maiolino, R., & Taniguchi, Y. 2011, *Astronomy and Astrophysics*, 527, A100
- Mernier, F., de Plaa, J., Kaastra, J. S., et al. 2017, *Astronomy and Astrophysics*, 603, A80
- Nagao, T., Marconi, A., & Maiolino, R. 2006, *Astronomy and Astrophysics*, 447, 157
- Nomoto, K., Kobayashi, C., & Tominaga, N. 2013, *Annual Review of Astronomy and Astrophysics*, 51, 457
- Novak, G. S., Ostriker, J. P., & Ciotti, L. 2011, *The Astrophysical Journal*, 737, 26
- Pellegrini, S. 2012, in *Hot Interstellar Matter in Elliptical Galaxies*, Vol. 378 (New York, NY: Springer New York), 21–54
- Portinari, L., Chiosi, C., & Bressan, A. 1998, *Astronomy and Astrophysics*, 334, 505
- Rice, W. K. M., Lodato, G., & Armitage, P. J. 2005, *Monthly Notices of the Royal Astronomical Society*, 364, L56
- Saitoh, T. R. 2017, *The Astronomical Journal*, 153, 85
- Sarzi, M., Falcón-Barroso, J., Davies, R. L., et al. 2006, *Monthly Notices of the Royal Astronomical Society*, 366, 1151
- Seitzzahl, I. R., Ciaraldi-Schoolmann, F., Rieke, F. K., et al. 2013, *Monthly Notices of the Royal Astronomical Society*, 429, 1156
- Stone, J. M., Gardiner, T. A., Teuben, P., Hawley, J. F., & Simon, J. B. 2008, *The Astrophysical Journal Supplement Series*, 178, 137
- Tan, J. C., & Blackman, E. G. 2005, *Monthly Notices of the Royal Astronomical Society*, 362, 983
- Tanaka, H., Takeuchi, T., & Ward, W. R. 2002, *The Astrophysical Journal*, 565, 1257
- Thomas, D., Maraston, C., Schawinski, K., Sarzi, M., & Silk, J. 2010, *Monthly Notices of the Royal Astronomical Society*, 404, 1775
- Thompson, T. A., Quataert, E., & Murray, N. 2005, *The Astrophysical Journal*, 630, 167
- Toomre, A. 1964, *The Astrophysical Journal*, 139, 1217
- Warner, C., Hamann, F., & Dietrich, M. 2003, *The Astrophysical Journal*, 596, 72
- Xu, F., Bian, F., Shen, Y., et al. 2018, *Monthly Notices of the Royal Astronomical Society*, 480, 345
- Yoon, D., Yuan, F., Gan, Z., et al. 2018, *The Astrophysical Journal*, 864, 6
- Yuan, F., Yoon, D., Li, Y., et al. 2018, *The Astrophysical Journal*, 857, 121